Sustainable Synthesis and Assembly of Biomass-Derived B/N Co-Doped Carbon Nanosheets with Ultrahigh Aspect Ratio for High-Performance Supercapacitors

Zheng Ling, Zhiyu Wang, Mengdi Zhang, Chang Yu, Gang Wang, Yanfeng Dong, Shaohong Liu, Yuwei Wang, and Jieshan Qiu**

The practical application of graphene has still been hindered by high cost and scarcity in supply. It boosts great interest in seeking for low-cost substitute of graphene for upcoming usage where extremely physical properties are not absolutely critical. The conversion of renewable biomass offers a great opportunity for sustainable and economic fabrication of 2D carbon nanostructures. However, large-scale production of carbon nanosheets with ultrahigh aspect ratio, satisfied electronic properties, and the capability of organized assembly like graphene has been rarely reported. In this work, a facile yet efficient approach for mass production of flexible boric/nitrogen co-doped carbon nanosheets with very thin thickness of 5–8 nm and ultrahigh aspect ratio of over 6000–10 000 is demonstrated by assembling the biomass molecule in long-range order on 2D hard template and subsequent annealing. The advantage of these doped carbon nanosheets over conventional products lies in that they can be readily assembled to multilevel architectures such as freestanding flexible thin film and ultralight aerogels with better electrical properties, which exhibit exceptional capacitive performance for supercapacitor application. The recyclability of boric acid template further reduces the discharge of the waste and processing cost, rendering high cost-effectiveness and environmental benignity for scalable production.

1. Introduction

2D carbon nanostructures have shown great potential in vast fields such as catalysis, biotechnology, energy storage and conversion due to the unique physiochemical and electronic properties in confined dimension of nanophase sp^2-hybridized carbon.[1] The planar geometries make them particularly compatible with the design of compact and space-saving electronics as ultrathin electrode or lightweight matrix materials.[2] Graphene is the representative of 2D carbon nanostructures with excellent flexibility, high conductivity, large lateral size but thin thickness. However, its practical application has still been hindered by high cost and scarcity in supply. This boosts great interest in seeking for low-cost substitute of graphene, for example, the carbon nanosheets, for upcoming applications where extreme physical properties are not absolutely critical. The conventional approaches based on molecular assembly or templating method mostly yield the pieces of carbon flakes with small lateral size of tens of nanometers to submicrometers,[3,4] which are hardly to be assembled into multilevel architectures such as thin films or aerogels via the crosslinkage of individual units. This drawback greatly reduces the value of carbon nanosheets as the low-cost substitute of graphene in specific areas such as flexible electronics and energy storage devices. For practical use, the facile approach for mass production of carbon nanosheets with ultrahigh aspect ratio (lateral size/thickness), satisfied electronic properties, and the capability of organized assembly is thus highly desired.

Supercapacitors are very appealing power sources for portable electronics, medical devices, and hybrid electrical vehicles (HEVs) owning to the merits of fast charge–discharging rate, superior lifespan, high power density, etc.[5] Porous carbon is the primary candidate of electrode materials in supercapacitors thank to intrinsically high conductivity, lightweight, and large surface areas for accumulating the ions via electric double layer (EDL) capacitance mechanism.[6,7] Nowadays, the performance of most available porous carbon electrodes is still far from the requirements of practical use due to the kinetic limitation in ionic transport in tortuous porosity at high current rate. Noted that the ion transport time (τ) is determined by ionic transport distance (L) in the relationship of $\tau = L^2/D$, where D refers to the ionic transport coefficient.[8] One can envision that carbon nanostructures with 2D open morphology and thin thickness of atomic/molecular level would possess intrinsic advantage over

Z. Ling, Prof. Z. Wang, M. Zhang, Dr. C. Yu, Dr. G. Wang, Y. Dong, S. Liu, Y. Wang, Prof. J. Qiu
Carbon Research Laboratory
Liaoning Key Lab for Energy Materials and Chemical Engineering
State Key Lab of Fine Chemicals
Dalian University of Technology
Dalian 116024, P. R. China
E-mail: zywang@dlut.edu.cn; jqiu@dlut.edu.cn

DOI: 10.1002/adfm.201504004

particulate-type system for fast charge storage.[4,8–10] Compared to 1D counterparts, 2D carbon nanostructures ensure superior electrical contact for charge transfer via enhanced topographical overlapping and interlock between individual units. Thus, excellent capacitive performance can be achieved by various materials such as graphene, microporous carbon nanoplates, porous graphene nanoplates, interconnected carbon nanosheets, graphene-based carbon nanosheets, etc.[4,8,10–12] Nevertheless, there is still huge room in satisfying the operational performance and processing cost of 2D carbon nanostructures in supercapacitors by rationally engineering the structure, chemical composition, and production strategy.

From a long-term perspective of environmental protection and sustainability, seeking for renewable carbon sources (e.g., biomass), along with developing facile yet economic process, is essential for practical application of carbon electrodes in energy storage. Recently, carbon nanosheets with large surface area, well-developed porosity, and good conductivity have been fabricated by the carbonization and activation of various biomass, such as hemp bast fiber or natural silk,[8,12] which exhibit high capacitances of 140–240 F g^{-1} in organic electrolyte. Layered silicate or montmorillnite templates have also been employed to guide the assembly and conversion behavior of biomass molecules (e.g., glucose, sucrose, gelatin, chitosan, etc.) via nanospace confinement in lamellar structures.[7,13] Despite the feasibility in tailoring the thickness, templating method is hardly to produce the nanosheets with large lateral size owing to the difficulty in homogenous diffusion of biomass molecules into deep inside of large template particles. Additionally, tedious removal of the templates with toxic etching agents (e.g., HF or NaOH) further brings severe concerns in safety, environmental protection, and cost issues.

Herein, we report a facile yet sustainable approach for large-scale production of B/N co-doped carbon nanosheets (denoted as B/N-CSs) with very thin thickness of 5–8 nm, ultrahigh aspect ratio of over 6000–10 000, and excellent flexibility by assembling the biomass molecule in long-range order on 2D hard template and subsequent annealing. Gelatin is chosen as carbon and nitrogen precursor because it is a naturally abundant and sustainable animal derivative composed of various proteins with a high average molecule weight of 50 000–80 000 and high N content (≈16%).[14] Boric acid is employed as both 2D template and boron source for B doping in carbon nanosheets, which can be readily recycled for repeated use by simply evaporative crystallization from final waste liquid.[15] This feature minimizes the discharge of the waste and significantly cuts the processing cost down, thereby being highly suitable for industrial production. When evaluated as the electrode in supercapacitors, the B/N-CSs deliver a high specific capacitance of 358 F g^{-1} at 0.1 A g^{-1}, outstanding rate capability, and long lifetime of 15 000 cycles. Like graphene, the B/N-CSs can be further assembled into easy-handled, freestanding flexible thin film electrodes without using any auxiliary additives thank to ultrahigh aspect ratio and flexible texture. They exhibit exceptional high-rate response to up to 100 A g^{-1} with a high specific capacitance of 189 F g^{-1}, as well as stable capacitance retention of 70% over a wide range of current densities from 0.2 to 100 A g^{-1}. After deeply cycling for as long as 15 000 cycles, the film electrodes can retain over 113% of the initial capacitance, highlighting the great promise in supercapacitor applications.

2. Results and Discussion

The synthetic strategy of B/N-CSs is schematically illustrated in **Scheme 1**a. The boric acid crystals are first formed by forced crystallization induced by continuous evaporation of its aqueous solution at 80 °C in the presence of gelatin. Guiding by the intrinsically layered structure, they preferentially grow into plate-like shape with exposed (002) plane during crystallization (Figure S1, Supporting Information). In this process, the gelatin molecule is assembled to the lateral plane of boric acid crystals, inhibiting its layer-by-layer growth and restacking along *c*-axis by which the boric acid plate gets thicker. Scanning electron microscopy (SEM) examination confirms the formation of the gelatin coated boric acid nanoplates with large lateral sizes of hundred micrometers but thin thicknesses of 100–200 nm, as shown in **Figure 1**a,b. The successful coating of gelatin layer on boric acid nanoplates is identified by dissolving gelatin-coated boric acid crystals in ethanol, resulting in curled gelatin film with soft texture (Figure S2, Supporting Information). After annealing at 900 °C in N_2, the gelatin layer is converted to carbon nanosheets via thermal-induced polycondensation and carbonization, while boric acid is decomposed to boron oxide

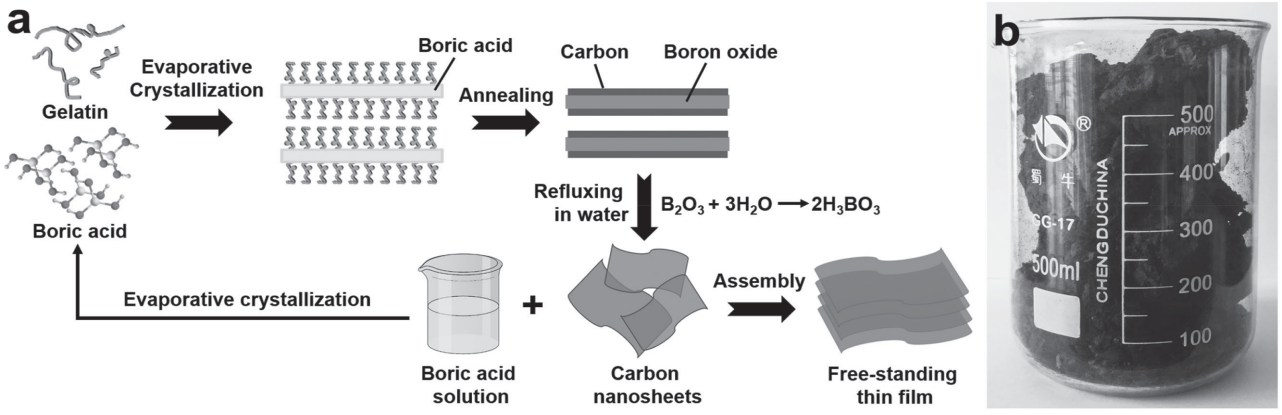

Scheme 1. a) Schematic illustration of sustainable synthesis and assembly of B/N-CSs; b) optical image of doped carbon nanosheets.

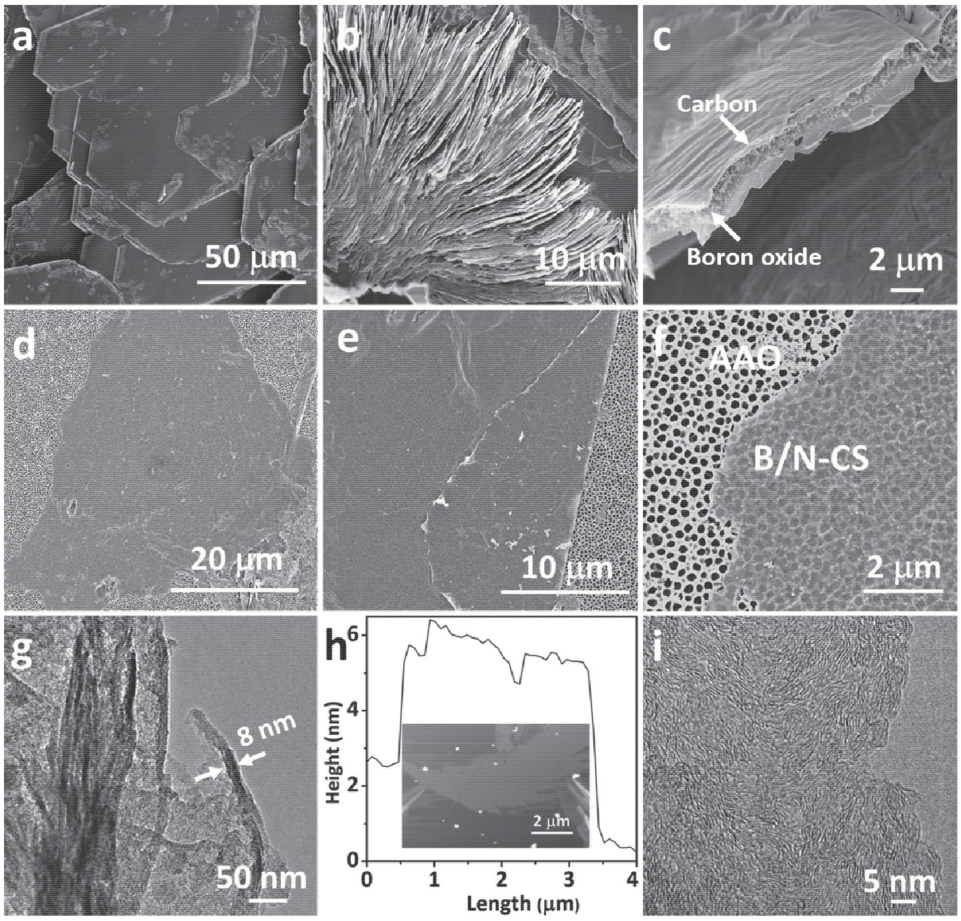

Figure 1. a) Top and b) cross-section SEM view of gelatin coated boric acid nanoplates; c) SEM image revealing the formation of carbon nanosheets on boron oxide nanoplate; d–f) SEM images of B/N-CSs supported on AAO membrane; g) cross-section TEM image of B/N-CSs; h) AFM image of a B/N-CS, indicating uniform thickness of 5.2–6.2 nm across the sheet; and i) HRTEM image of B/N-CSs.

(Figure 1c). Meanwhile, the B and N heteroatoms are also incorporated into carbon nanosheets upon heating. The boron oxide in the sample can be readily washed away by refluxing in boiling water to form boric acid, eventually giving rise to pure B/N-CSs with gram-scale yield (Scheme 1b). After the whole process, over 90% of boric acid with high purity can be recycled by simply evaporating the waste liquid, and be repeatedly used as template material for B/N-CS production, indicative of the fascinating sustainability of this strategy (Figure S3, Supporting Information).

SEM analysis shows that the B/N-CS sample possesses flat sheet-like morphology with an impressive lateral size of over 50 μm, as shown in Figure 1d. The sheet can be folded face to face without cracking, showing excellent structural flexibility (Figure 1e). When being placed on a porous anodic aluminum oxide (AAO) membrane, the B/N-CSs are largely transparent under electron beam to reveal the holes of underlying AAO membrane in virtue of thin thickness (Figure 1f). To figure out the accurate thickness of B/N-CSs, they are embedded into the epoxy resin and cut into thin slice using a microtome. The cross-section transmission electron microscopy (TEM) image of B/N-CSs indicates the thickness of the nanosheets is only 5–8 nm (Figure 1g and Figure S4a, Supporting Information), which is about the same thickness of the graphene with 10–20 single layers. Despite the very thin thickness, the B/N-CSs have a flat surface without apparent wrinkles, as shown in Figure S4b (Supporting Information). The atomic force microscope (AFM) analysis confirms the uniform thickness of 5.2–6.2 nm across the carbon nanosheet (Figure 1h), being consistent with TEM observation. The aspect ratio of B/N-CSs is thus estimated to be as high as 6200–10 000. High-resolution TEM (HRTEM) analysis reveals that the sheets consist of numerous short-range-ordered graphitic regions of 10–20 nm (Figure 1i), indicative of their polycrystalline texture.

The structural characteristics of B/N-CSs are determined by X-ray powder diffraction (XRD), as shown in **Figure 2**a. The broad peak centered at around 26° confirms the formation of polycrystalline carbon nanosheets, being in good agreement with HRTEM characterization. The pronounced peaks from boron oxides formed during annealing disappear completely, showing high efficiency of template removal by refluxing in boiling water. The N_2 adsorption–desorption test shows that the B/N-CSs have a large Brunauer–Emmett–Teller (BET) specific surface area of 416 m^2 g^{-1} with a total pore volume of 0.76 cm^3 g^{-1} (Figure 2b), which are larger than the value of reduced graphene oxide made by Hummer's method.[16] X-ray

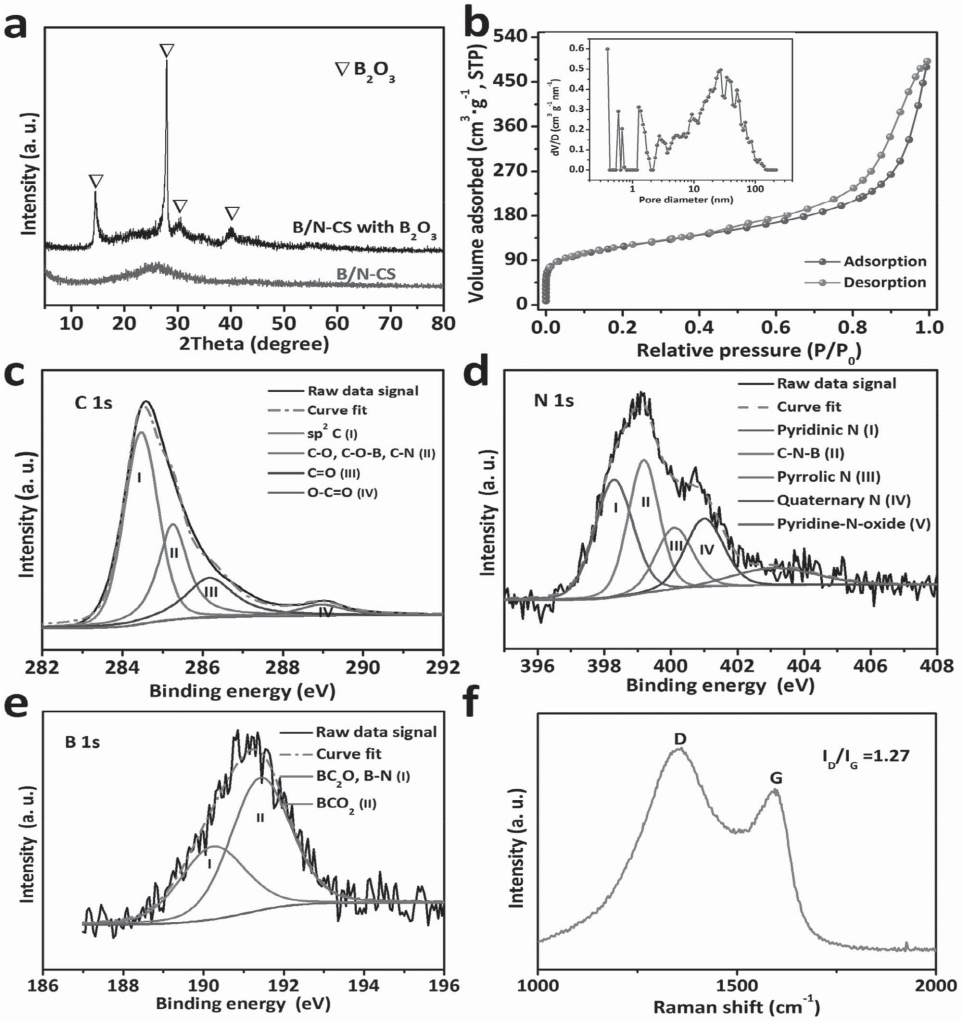

Figure 2. a) XRD profiles of the sample before and after refluxing in boiling water; b) N_2 sorption isotherm of B/N-CSs. The inset is the pore size distribution; c) C 1s, d) N 1s, e) B 1s XPS spectra of B/N-CSs; f) Raman spectrum of B/N-CSs.

photoelectron spectroscopy (XPS) survey scan confirms the presence of carbon, nitrogen, boron, and oxygen elements in the sample (Figure S5a, Supporting Information). The C1s signal is centered at 284.5 eV, showing that the nanosheets are predominantly of sp^2-hybridized carbon.[17,18] It can be divided into two sharp peaks from sp^2 C–C (284.5 eV) and C–O/C–N/C–O–B (285.3 eV) bonds, as well as the other two small ones from C=O (286.2 eV) and O–C=O (289.0 eV) bonds (Figure 2c).[19] The N1s spectrum (Figure 2d) visualizes the presence of five forms of N, namely, pyrrolic N (400.1 eV), pyridinic N (398.3 eV), quaternary N (401.0 eV), C–N–B (399.2 eV), and pyridine-N-oxide (403.3 eV).[20] The high-resolution B1s spectrum (Figure 2e) can be deconvoluted into two different signals with binding energies of 190.3 and 191.4 eV that correspond to B–C_2O/B–N and B–CO_2 bonds, respectively.[21] The B content in B/N-CSs is 3.3 wt%, measured by inductively coupled plasma optical emission spectroscopy (ICP-OES), while the N content in the same sample is 8.6 wt% as measured by elemental analysis. The above results suggest that the B and N atoms have been incorporated into the sp^2 carbon frame. Their presence may significantly change the electronic structure and density of state of the carbon, initiating the faradic reactions and leading to larger value of the interfacial capacitance.[17,22] The heteroatom doping simultaneously creates extra surface defects on carbon nanosheet for the adsorption of moisture, atmospheric oxygen or CO_2, leading to a high content of oxygen (10.1 at%) in the sample (Figure S5b, Supporting Information).[20,23] Figure 2f shows the Raman spectrum of B/N-CSs. The band at around 1590 cm^{-1} (G band) corresponds to the in-plane vibration of sp^2 carbon atoms, and the band at around 1350 cm^{-1} (D band) mainly reflects the structural defects in the graphitic structure. The intensity ratio between two bands (I_D/I_G) is around 1.27, revealing the domination of disordered structure of the nanosheets.

The ultrahigh aspect ratio plus flexible texture of B/N-CSs allows them to be directly assembled into easy-handled free-standing thin film by vacuum filtration without using any auxiliary additives (**Figure 3**a). This is hardly to be achieved for conventional carbon nanosheets with small lateral size and larger thickness except the graphene. The large overlapping

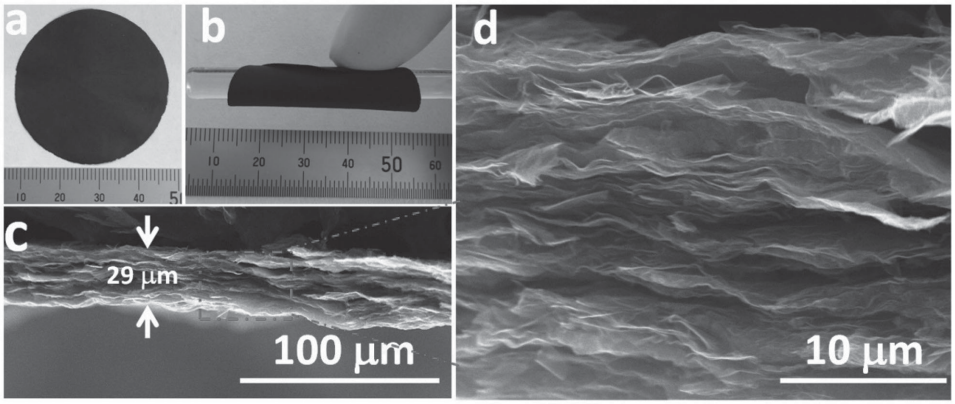

Figure 3. a) Optical image of a freestanding B/N-CS film; b) a flexible film wrapping around a glass rod; c,d) cross-section SEM images of a B/N-CS film with a thickness of 29 μm.

area between individual nanosheets has the great benefit to keep the mechanical properties and internal electrical contact of the film being unaffected upon deforming. As a result, the B/N-CS film can be readily bent up to 180° or rolled up without detectable damage (Figure 3b). The thickness of the flexible B/N-CS film can be tailored by tuning the filtrated volume of B/N-CSs suspension with a given concentration. As an example, a film with a thickness of around 29 μm is shown in Figure 3c. The cross-section SEM images of the film reveal a well-aligned layered structure of the nanosheets throughout the entire film (Figure 3d), which provides a less tortuous diffusion pathway for ion transport than that of the particulate electrodes. Compared to B/N-CS powder, the assembled film exhibits slightly lower surface area of 393 m^2 g^{-1}. Furthermore, the B/N-CSs can also be assembled into 3D aerogels with a very low density of 4.81 mg cm^{-3} and rich porosity of over 99% due to strong interaction by entanglement with each other (Figure S6, Supporting Information). The density of B/N-CS aerogels is comparable to that of ultralight graphene aerogels (typically 3–5 mg cm^{-3}),[24] thus being regarded as a kind of new ultralight material.

The capacitive performance of B/N-CSs was evaluated using cyclic voltammetry (CV), galvanostatic charge–discharge (GCD), and electrochemical impedance spectroscopy (EIS) techniques in 1 M H_2SO_4 aqueous solution in a three-electrode system. Ti meshes are used as the current collectors for electrolyte of H_2SO_4, which exhibit negligible specific capacitances (<10 F g^{-1} at a scan rate of 5 mV s^{-1}), as shown in Figure S7a (Supporting Information). A partial negative voltage of –0.7 to 0.3 V (vs Hg/Hg_2SO_4) is adopted for the test to avoid the oxidation of the carbon in H_2SO_4 electrolyte. **Figure 4**a,b shows the CV curves of B/N-CSs and their freestanding film at various scan rates of 5–100 mV s^{-1}, respectively. They exhibit similar rectangular-like shape along with a pair of redox peaks centered at around –0.2 V (vs Hg/Hg_2SO_4). These redox peaks are a fingerprint feature of reversible faradic reactions that are associated with electrochemically active functionalities such as B and N heteroatoms, as well as oxygen-containing functionalities on nanosheet surface.[17,25] However, they are hardly to be distinguished due to severe overlapping of redox peaks in CVs. The capacitive behavior of B/N-CS electrodes is thus believed to be a combined contribution of the pseudocapacitance and EDL capacitance. For the B/N-CS film, the CV curves almost remain the same in shape as the scan rate increased from 5 to 100 mV s^{-1}, showing fast kinetics for EDL formation and faradic reactions over the nanosheets. The GCD profiles of B/N-CSs and the B/N-CS film are shown in Figures S8 and S9 (Supporting Information). For both samples, the symmetrical shapes of the GCD curves indicate a high degree of the reversibility for charge storage and delivery. The electrodes made of B/N-CS powder deliver an impressive specific capacitance of 358 F g^{-1} at a current density of 0.1 A g^{-1} (Figure 4c), corresponding to a BET area-normalized capacitance of 86 μF cm^{-2}. Even at a high current density of up to 30 A g^{-1}, they can still exhibit a superior specific capacitance of 267 F g^{-1} and BET area-normalized capacitance of 64 μF cm^{-2}. This value is much higher than the capacitance that could be realized from EDL charge storage on carbon surface (typically 10–30 μF cm^{-2}).[26] After assembly, the B/N-CS film electrodes exhibit even better rate capability despite the lower specific capacitance at moderate current densities. Stable capacitance retention of 90% is achieved as the current densities increased from 1 A g^{-1} (210 F g^{-1}) to 100 A g^{-1} (189 F g^{-1}), and a constant value of 70% compared to the capacitance at 0.1 A g^{-1} (268 F g^{-1}) can be maintained over a wide range of the current densities from 0.1 to 100 A g^{-1} (Figure 4c), highlighting an excellent power capability. When cycling in 6 M KOH electrolyte, the B/N-CS film electrodes also exhibit excellent rate capability as the current densities increased from 0.1 A g^{-1} (223 F g^{-1}, 57 μF cm^{-2}) to 100 A g^{-1} (140 F g^{-1}, 36 μF cm^{-2}), as shown in **Figure 5**. In this case, Ni foams are used as the current collectors for KOH electrolyte, which exhibit negligible specific capacitances (<10 F g^{-1} at a scan rate of 5 mV s^{-1}), as shown in Figure S7b (Supporting Information). Such an excellent performance is superior to most of the reported doped carbon electrode materials in aqueous electrolyte, as compared in Table S1 (Supporting Information).

In addition to high-rate capability, the cycling life is also of great importance for long-life supercapacitors. For the electrodes made of B/N-CSs and their freestanding film, the capacitance increases gradually to reach 105% and 113% of the initial value within 10 000 and 15 000 cycles, respectively (Figure 4d). Similar phenomena of capacitance rise with cycling have also been reported in other porous carbon electrodes in

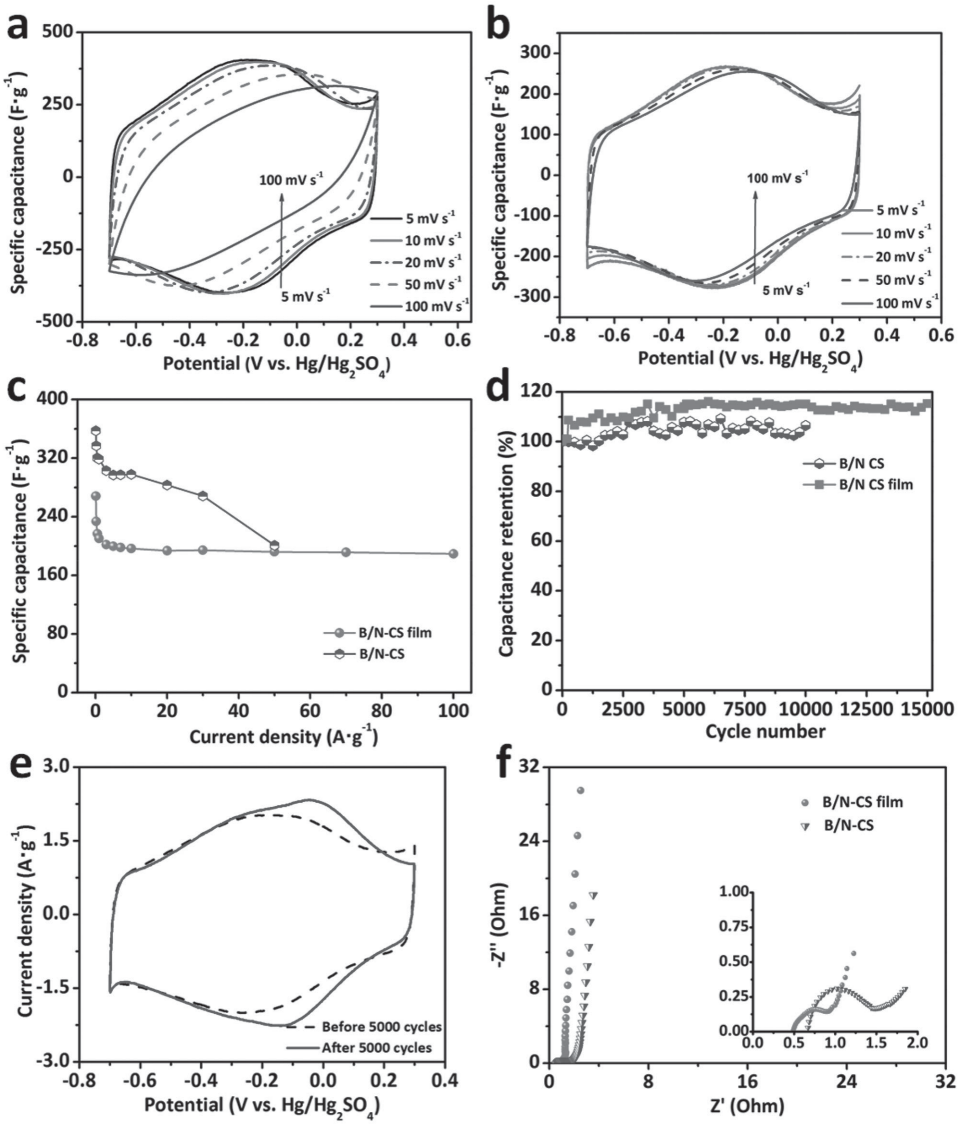

Figure 4. a) CV curves of the electrode made of B/N-CS powder at scan rate of 5–100 mV s^{-1}; b) CV curves of B/N-CS film electrode at scan rate of 5–100 mV s^{-1}; c) specific capacitance of the electrode made of B/N-CS powder and B/N-CS film at different current densities; d) cycling stability of the electrode made of B/N-CS powder and B/N-CS film at 5 A g^{-1}; e) CV curves of the electrode made of B/N-CS powder before and after 5000 cycles, which are obtained at a scan rate of 5 mV s^{-1}; f) Nyquist plots of the electrode made of B/N-CS powder and B/N-CS film in the frequency ranging from 100 kHz to 10 mHz.

supercapacitors, which is ascribed to the electroactivation process and/or the improved wettability of the electrodes.[27,28] To investigate this point, the CV curves before and after 5000 cycles are compared for the electrodes made of B/N-CSs and their film, as shown in Figure 4e and Figure S10 (Supporting Information). The significantly increased intensity of the redox peaks after deep cycling indicates greatly enhanced faradic reactions for charge storage, implying the electroactivation effect should be responsible for the capacitance increase. In addition, other reasons such as enhanced wettability and improved accessibility of the pores may also contribute to the capacitance rise during repeated cycling, which is not uncommon for carbon electrodes in supercapacitors.[27,29]

The enhanced kinetics for ion transport and charge transfer in B/N-CSs and their film electrodes is proven by EIS, as shown in Figure 4f. The nearly vertical line in low frequency region of Nyquist plots indicates the fast ion diffusion and migration in both electrodes. In relatively high frequency region, the semicircles with a small diameter in Nyquist plots is attributed to the charge-transfer resistance during faradic reactions.[30] Specifically, the B/N-CS film electrode exhibits greatly reduced charge transfer resistance than that of the electrode made of B/N-CS powders as a result of enhanced electrical contact between the overlapping sheets. Four-probe analysis shows that the electrical conductivity of B/N-CSs is 9.8 S m^{-1}, which can be increased sixfolds (58.8 S m^{-1}) by assembling to freestanding

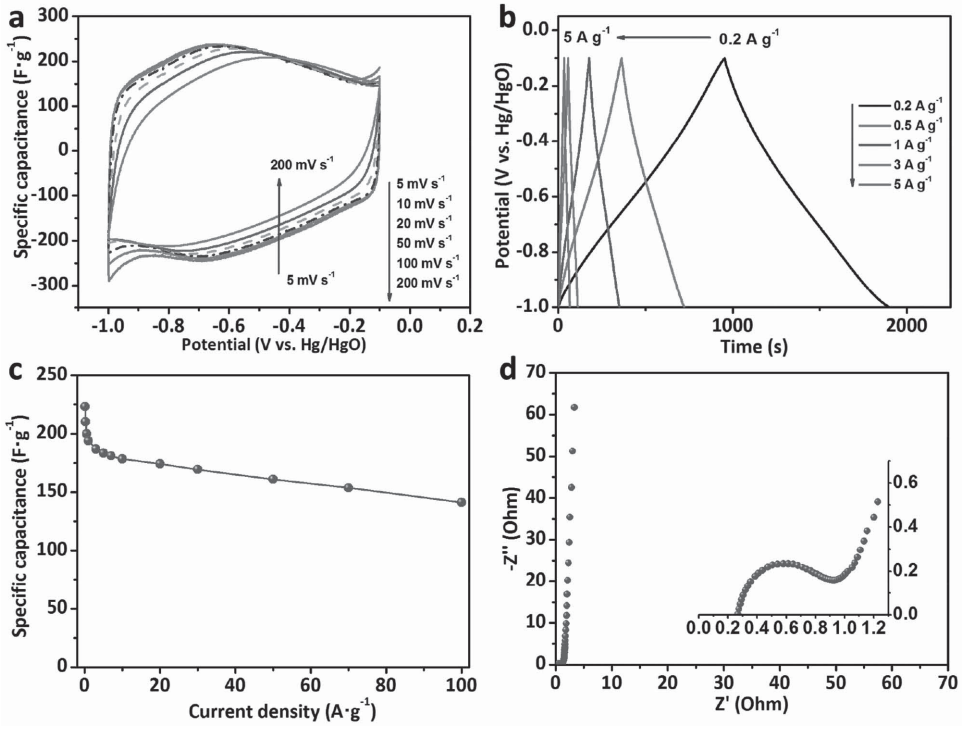

Figure 5. Electrochemical performance of B/N-CS film electrodes in 6 M KOH electrolyte. a) CV curves at scan rate of 5–200 mV s^{-1}; b) galvanostatic charge–discharge curves; c) specific capacitance at different current densities; d) Nyquist plots in the frequency ranging from 100 kHz to 10 mHz.

film. This value is comparable to or even higher than that of reduced graphene oxides or chemically modified graphene, as well as their freestanding films, as compared in Table S2 (Supporting Information).[31] As a result, the B/N-CS films exhibit significantly enhanced high-rate capability to their powder counterpart (Figure 4a–c).

Two-electrode cell tests of the B/N-CS film were carried out in 1 M H_2SO_4 electrolyte to further characterize the electrochemical performance, as shown in **Figure 6**. The CV curves exhibit the rectangular shaped voltammetry characteristics within different voltage windows of 0.8–1.2 V (Figure 6a). The supercapacitor made of B/N-CS film electrodes delivers a specific capacitance of 240 and 230 F g^{-1} at 0.1 A g^{-1} within the voltage windows of 0.8 and 1.0 V, respectively (Figure 6b). Comparable capacitance retention of 50% at varied current densities of 0.2–30 A g^{-1} is achieved within the same voltage windows. The Ragone plots show that the energy density of the supercapacitor made of B/N-CS film electrodes can reach 8 Wh kg^{-1} and the power density can be 6 kW kg^{-1} (Figure 6d). The moderate energy and power density is related to the high mass loading of the electrodes employed.

3. Conclusions

In conclusion, we have developed a scalable and economic approach for sustainable production of B/N co-doped carbon nanosheets by assembling the gelatin molecule in long-range order on 2D crystals of boric acid followed by annealing. The doped carbon nanosheets feature with very thin thickness, ultrahigh aspect ratio, and excellent flexibility, enabling the assembly to flexible freestanding thin films or ultralight aerogels. Both the doped carbon nanosheets and the assembled films show excellent performance as supercapacitor electrodes, as characterized by high capacitance from combined contribution of the pseudocapacitance and EDL capacitance, excellent high-rate capability of up to 100 A g^{-1}, and long lifetime of over 10 000–15 000 cycles with 105%–113% capacitance retention. Remarkably, the boric acid template can be largely recycled by the evaporation of final waste liquid for repeated production of doped carbon nanosheets. It makes the process highly cost-effective and environmentally benign for large-scale production, especially while combining with cheap biomass precursors.

4. Experimental Section

Material Preparation: In a typical run, boric acid (20 g) was dissolved into deionized water at 80 °C, followed by adding the gelatin (2 g) under magnetic stirring. The mixture solution was kept at 80 °C under stirring until the water was evaporated. The resultant composite was then annealed at 900 °C for 1 h at a ramp rate of 5 °C min^{-1} in N_2 flow, yielding a black monolithic product. After refluxing in deionized water for 1.5 h, carbon nanosheets were harvested by several centrifugation-rinsing cycles, followed by freeze-drying. The production can be easily scaled up to 5–10 folds. For the assembly, the suspension of doped carbon nanosheets was subjected to vacuum filtration by using a 0.22 μm cellulose ester filter paper to make free-standing film.

Material Characterization: The morphology of the samples was characterized with field-emission scanning electron microscopy (FESEM, FEI NovaNano SEM 450) and TEM (JEOL JEM-2100, Philips Tecnai G220). The samples for TEM observation of the cross section of carbon

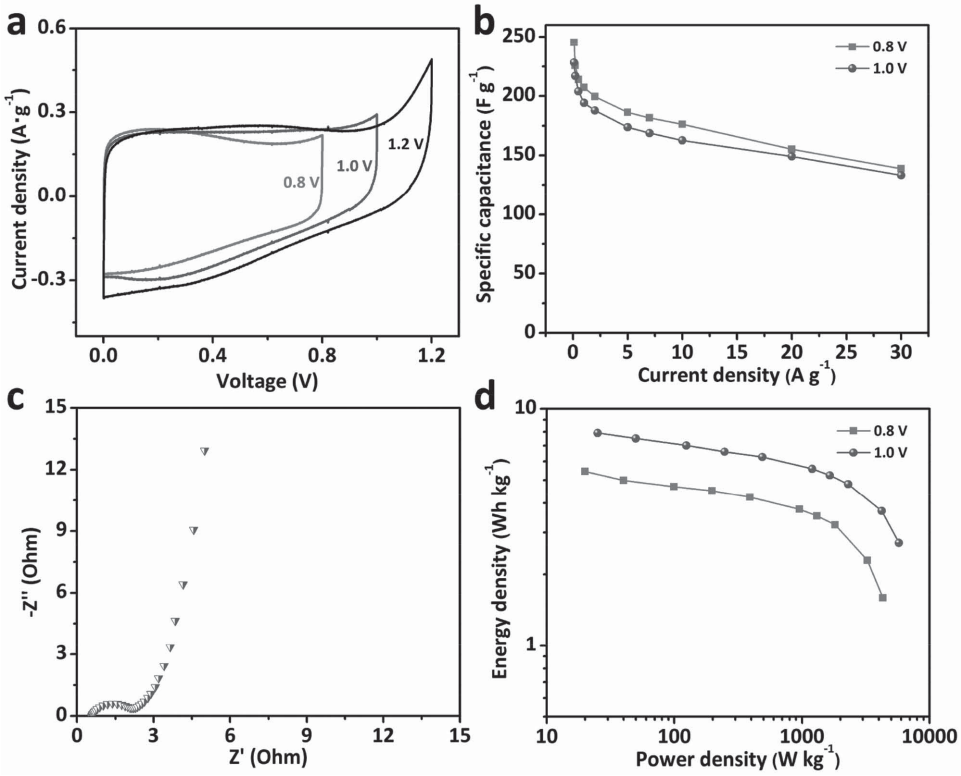

Figure 6. Electrochemical performance of the symmetrical supercapacitor assembled from B/N-CS film electrodes. a) CV curves at a scan rate of 2 mV s^{-1} within different voltage windows; b) rate capability at varied current densities within different voltage windows; c) Nyquist plot in the frequency ranging from 100 kHz to 10 mHz; d) Ragone plots within different voltage windows.

nanosheets were prepared by cutting the epoxy resin embedded with B/N-CS film into thin slice using a microtome, which were supported on a lacey-carbon coated Cu grid. The thickness of B/N-CSs was also analyzed by AFM (Park Systems, XE-70) using a tapping mode. The texture and surface properties of the samples were measured by Micrometrics ASAP 2020 Surface Area and Porosity Analyzer at 77 K and ESCALAB MK II X-ray photoelectron spectrometer. The microstructure of the samples was analyzed by type D/Max-III X-ray spectrometer with Cu Kα radiation (XRD, λ = 1.5406 Å) and Raman spectroscopy (Thermal Scientific DXR with an excitation wavelength of 532 nm). The composition of the samples was examined by a vario EL III Elemental Analyzer (Elementar, Germany) and ICP-OES (Optima 2000DV, PerkinElmer, Inc.). The electrical conductivity of the samples was recorded with a standard four-probe analyzer.

Electrochemical Test: The electrochemical measurements were carried out in a three-electrode system with Pt foil as the counter electrode, Hg/Hg_2SO_4 as the reference electrode in 1 M H_2SO_4, or Hg/HgO as the reference electrode in 6 M KOH at room temperature. The working electrode consists of B/N-CS powder, carbon black (Super-P), and polytetrafluoroethylene in a weight ratio of 85:10:5. The B/N-CS films were directly used as working electrode without adding the binder and conducting agents. The area of the electrodes is ≈1 cm^2 with mass loading of 3.8–4.5 mg. Ti mesh or Ni foam was used as the current collector in acidic or alkaline medium, respectively. CV studies were conducted using a CHI 660D electrochemical workstation between –0.7 and 0.3 V (vs Hg/Hg_2SO_4) or –1.0 and –0.1 V (vs Hg/HgO) at increasing sweep rates from 5 to 100 mV s^{-1}. The gravimetric specific capacitance of the active materials was calculated according to the following equation

$$C = \frac{\int I\,dV}{\nu m} \quad (1)$$

where C is the gravimetric specific capacitance (F g^{-1}), I is the response current density (A g^{-1}), ν is the potential scanning rate (V s^{-1}), and m is the active mass in the electrode (g).

GCD tests were conducted with a CHI 660D electrochemical workstation at the current densities of 0.1–100 A g^{-1} between –0.7 and 0.3 V (vs Hg/Hg_2SO_4). The gravimetric capacitance (F g^{-1}) was calculated from constant charge/discharge curves by following formula

$$C = \frac{I_{cons}t}{m\Delta V} \quad (2)$$

where I_{cons} is the constant discharge current (A), t is the discharge time (s), m is the active mass in the electrode (g), and ΔV is the voltage range.

The cycling stability was studied using a LAND CT2001A battery tester at 5 A g^{-1} within a cut-off voltage window of –0.7 to 0.3 V (vs Hg/Hg_2SO_4). EIS was performed using a CHI 660D electrochemistry workstation by applying AC amplitude of 5 mV over the frequency range from 100 kHz to 10 mHz.

For two-electrode tests, two pieces of B/N-CS film with identical mass were symmetrically assembled with a nonwoven fabric as separator. CV studies were conducted within different voltage windows of 0.0–0.8, 0.0–1.0, and 0.0–1.2 V at increasing sweep rates from 5 to 100 mV s^{-1}. GCD tests were conducted at the current densities of 0.1–30 A g^{-1} between 0.0–0.8 and 0.0–1.0 V. The energy density E (Wh kg^{-1}) and power density P (W kg^{-1}) for the Ragone plots were calculated via the following equations based on the total active mass in supercapacitors

$$E = \frac{CV^2}{8\times 3.6} \quad (3)$$

$$P = \frac{E}{t} \quad (4)$$

where V is the voltage after ohmic drop (V) and t is the discharge time (h).

Supporting Information

Supporting Information is available from the Wiley Online Library or from the author.

Acknowledgements

The authors sincerely appreciate Prof. Yury Gogotsi and Dr. Mengqiang Zhao from Drexel University for the help with cross-section TEM characterization. This work was partly supported by the NSFC (Nos. 21336001 and 51522203), the start-up grant from Dalian University of Technology (No. DUT14RC(3)091) and Education Department of Liaoning Province (No. L2014029).

Received: September 19, 2015
Published online: November 24, 2015

[1] a) G. Xie, K. Zhang, B. Guo, Q. Liu, L. Fang, J. R. Gong, *Adv. Mater.* **2013**, *25*, 3820; b) P. C. Gao, W. Y. Tsai, B. Daffos, P. L. Taberna, C. R. Pérez, Y. Gogotsi, P. Simon, F. Favier, *Nano Energy* **2015**, *12*, 197.

[2] a) X. Peng, L. Peng, C. Wu, Y. Xie, *Chem. Soc. Rev.* **2014**, *43*, 3303; b) X. Yang, C. Cheng, Y. Wang, L. Qiu, D. Li, *Science* **2013**, *341*, 534.

[3] a) P. Angelova, H. Vieker, N. E. Weber, D. Matei, O. Reimer, I. Meier, S. Kurasch, J. Biskupek, D. Lorbach, K. Wunderlich, L. Chen, A. Terfort, M. Klapper, K. Müllen, U. Kaiser, A. Gölzhäuser, A. Turchanin, *ACS Nano* **2013**, *7*, 6489; b) X. H. Li, S. Kurasch, U. Kaiser, M. Antonietti, *Angew. Chem., Int. Ed.* **2012**, *51*, 9689; c) X. Zheng, W. Lv, Y. Tao, J. Shao, C. Zhang, D. Liu, J. Luo, D. W. Wang, Q. H. Yang, *Chem. Mater.* **2014**, *26*, 6896.

[4] X. Liu, M. Antonietti, *Adv. Mater.* **2013**, *25*, 6284.

[5] a) P. Simon, Y. Gogotsi, *Acc. Chem. Res.* **2012**, *46*, 1094; b) F. Béguin, V. Presser, A. Balducci, E. Frackowiak, *Adv. Mater.* **2014**, *26*, 2219; c) V. Augustyn, P. Simon, B. Dunn, *Energy Environ. Sci.* **2014**, *7*, 1597.

[6] L. Wei, M. Sevilla, A. B. Fuertes, R. Mokaya, G. Yushin, *Adv. Energy Mater.* **2011**, *1*, 356.

[7] X. Fan, C. Yu, J. Yang, Z. Ling, C. Hu, M. Zhang, J. Qiu, *Adv. Energy Mater.* **2015**, *5*, 1401761.

[8] H. Wang, Z. Xu, A. Kohandehghan, Z. Li, K. Cui, X. Tan, T. J. Stephenson, C. K. King'ondu, C. M. B. Holt, B. C. Olsen, J. K. Tak, D. Harfield, A. O. Anyia, D. Mitlin, *ACS Nano* **2013**, *7*, 5131.

[9] a) M. Sevilla, A. B. Fuertes, *ACS Nano* **2014**, *8*, 5069; b) J. Li, R. Yao, J. Bai, C. Cao, *ChemPlusChem* **2013**, *78*, 797.

[10] X. Wang, Y. Zhang, C. Zhi, X. Wang, D. Tang, Y. Xu, Q. Weng, X. Jiang, M. Mitome, D. Golberg, Y. Bando, *Nat. Commun.* **2013**, *4*, 2095.

[11] Y. Zhu, S. Murali, M. D. Stoller, K. J. Ganesh, W. Cai, P. J. Ferreira, A. Pirkle, R. M. Wallace, K. A. Cychosz, M. Thommes, D. Su, E. A. Stach, R. S. Ruoff, *Science* **2011**, *332*, 1537.

[12] Y. S. Yun, S. Y. Cho, J. Shim, B. H. Kim, S. J. Chang, S. J. Baek, Y. S. Huh, Y. Tak, Y. W. Park, S. Park, H. J. Jin, *Adv. Mater.* **2013**, *25*, 1993.

[13] a) A. Bakandritsos, T. Steriotis, D. Petridis, *Chem. Mater.* **2004**, *16*, 1551; b) K. K. R. Datta, D. Jagadeesan, C. Kulkarni, A. Kamath, R. Datta, M. Eswaramoorthy, *Angew. Chem., Int. Ed.* **2011**, *50*, 3929.

[14] a) G. Nam, J. Park, S. T. Kim, D. B. Shin, N. Park, Y. Kim, J. S. Lee, J. Cho, *Nano Lett.* **2014**, *14*, 1870; b) G. P. Mane, S. N. Talapaneni, C. Anand, S. Varghese, H. Iwai, Q. Ji, K. Ariga, T. Mori, A. Vinu, *Adv. Funct. Mater.* **2012**, *22*, 3596; c) B. Xu, S. Hou, F. Zhang, G. Cao, M. Chu, Y. Yang, *J. Electroanal. Chem.* **2014**, *712*, 146; d) B. Yi, X. Chen, B. Zeng, K. Guo, Z. Wan, Q. Qian, H. Yan, J. Chen, *J. Porous Mater.* **2012**, *19*, 37; e) H. Li, D. Q. Wang, H. L. Chen, B. L. Liu, L. Z. Gao, *Macromol. Biosci.* **2003**, *3*, 720.

[15] Z. Ling, G. Wang, M. Zhang, X. Fan, C. Yu, J. Yang, N. Xiao, J. Qiu, *Nanoscale* **2015**, *7*, 5120.

[16] Y. Zhu, S. Murali, W. Cai, X. Li, J. W. Suk, J. R. Potts, R. S. Ruoff, *Adv. Mater.* **2010**, *22*, 3906.

[17] Z. S. Wu, A. Winter, L. Chen, Y. Sun, A. Turchanin, X. Feng, K. Müllen, *Adv. Mater.* **2012**, *24*, 5130.

[18] Y. Zheng, Y. Jiao, L. Ge, M. Jaroniec, S. Z. Qiao, *Angew. Chem., Int. Ed.* **2013**, *52*, 3110.

[19] S. Wang, E. Iyyamperumal, A. Roy, Y. Xue, D. Yu, L. Dai, *Angew. Chem., Int. Ed.* **2011**, *50*, 11756.

[20] D. Hulicova-Jurcakova, M. Seredych, G. Q. Lu, T. J. Bandosz, *Adv. Funct. Mater.* **2009**, *19*, 438.

[21] a) X. H. Li, M. Antonietti, *Angew. Chem., Int. Ed.* **2013**, *52*, 4572; b) L. Ci, L. Song, C. Jin, D. Jariwala, D. Wu, Y. Li, A. Srivastava, Z. F. Wang, K. Storr, L. Balicas, F. Liu, P. M. Ajayan, *Nat. Mater.* **2010**, *9*, 430; c) W. Lei, D. Portehault, R. Dimova, M. Antonietti, *J. Am. Chem. Soc.* **2011**, *133*, 7121.

[22] a) J. Han, L. L. Zhang, S. Lee, J. Oh, K.-S. Lee, J. R. Potts, J. Ji, X. Zhao, R. S. Ruoff, S. Park, *ACS Nano* **2013**, *7*, 19; b) J. H. Hou, C. B. Cao, F. Idrees, X. L. Ma, *ACS Nano* **2015**, DOI: 10.1021/nn506394r; c) L. Niu, Z. Li, W. Hong, J. Sun, Z. Wang, L. Ma, J. Wang, S. Yang, *Electrochim. Acta* **2013**, *108*, 666.

[23] a) Y. Shao, S. Zhang, M. H. Engelhard, G. Li, G. Shao, Y. Wang, J. Liu, I. A. Aksay, Y. Lin, *J. Mater. Chem.* **2010**, *20*, 7491; b) C. Moreno-Castilla, M. B. Dawidziuk, F. Carrasco-Marin, Z. Zapata-Benabithe, *Carbon* **2011**, *49*, 3808.

[24] H. Hu, Z. Zhao, W. Wan, Y. Gogotsi, J. Qiu, *Adv. Mater.* **2013**, *25*, 2219.

[25] a) E. Raymundo-Piñero, F. Leroux, F. Béguin, *Adv. Mater.* **2006**, *18*, 1877; b) M. Inagaki, H. Konno, O. Tanaike, *J. Power Sources* **2010**, *195*, 7880.

[26] a) L. L. Zhang, X. S. Zhao, *Chem. Soc. Rev.* **2009**, *38*, 2520; b) L. L. Zhang, R. Zhou, X. S. Zhao, *J. Mater. Chem.* **2010**, *20*, 5983.

[27] a) Q. Cheng, J. Tang, J. Ma, H. Zhang, N. Shinya, L.-C. Qin, *Carbon* **2011**, *49*, 2917; b) G. Wang, Z. Ling, C. Li, Q. Dong, B. Qian, J. Qiu, *Electrochem. Commun.* **2013**, *31*, 31.

[28] V. Ganesh, S. Pitchumani, V. Lakshminarayanan, *J. Power Sources* **2006**, *158*, 1523.

[29] Y. Fang, B. Luo, Y. Jia, X. Li, B. Wang, Q. Song, F. Kang, L. Zhi, *Adv. Mater.* **2012**, *24*, 6348.

[30] X. Fan, C. Yu, Z. Ling, J. Yang, J. Qiu, *ACS Appl. Mater. Interfaces* **2013**, *5*, 2104.

[31] S. Park, R. S. Ruoff, *Nat. Nanotechnol.* **2009**, *4*, 217.